ACS NANO

www.acsnano.org

ARTICLE

Single-Atom Cu Anchored on Carbon Nitride as a Bifunctional Glucose Oxidase and Peroxidase Nanozyme for Antibacterial Therapy

Fan Wu, Yaran Wang, Yuanfeng Li, Linqi Shi,* Lu Yuan, Yijin Ren, Henny C. van der Mei,* and Yong Liu*

Cite This: *ACS Nano* 2025, 19, 10816−10828

Read Online

ACCESS | Metrics & More | Article Recommendations | Supporting Information

ABSTRACT: **A very promising strategy to avoid bacterial drug resistance is to replace antibiotics with artificial nanozymes, but this has not yet been translated to the clinic. Here, we construct a single-atom nanozyme using graphitic carbon nitride nanosheets modified by copper (Cu-*g*-C_3N_4). This Cu-*g*-C_3N_4 nanosheet possesses both glucose oxidase-like and peroxidase-like activities responsible for reactive-oxygen-species generation by a cascade reaction to eradicate Gram-positive and Gram-negative multidrug-resistant bacteria. Cu-*g*-C_3N_4 is introduced into polycaprolactone (PCL) by electrospinning to obtain (Cu-*g*-C_3N_4/PCL) nanofibers, which can be used as a dressing for bacterially infected wounds. It is demonstrated that Cu-*g*-C_3N_4/PCL nanofiber dressings can eradicate bacterial infections and accelerate wound healing in a mouse model with a skin wound.**

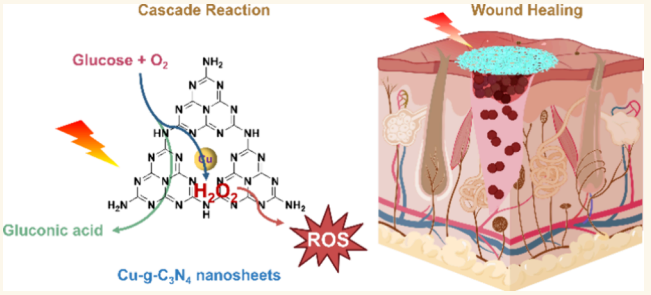

KEYWORDS: *single-atom nanozyme, cascade reaction, bacterial infection, biofilm, wound dressing*

INTRODUCTION

Antibiotic resistance represents an urgent threat to global public health.[1,2] Bacteria tend to adhere to a surface such as damaged tissue or medical devices, which can cause chronic, persistent, or biomaterials-associated infections.[3,4] Usually, these adhered bacteria produce polysaccharides, proteins, and eDNA, forming a matrix, in which they are encapsulated, known as a biofilm.[5−8] Bacteria residing within a biofilm have many benefits, like shielding them from environmental stress, including antimicrobial challenges and the host immune system. Therefore, a much higher antibiotic dose is required to eradicate bacteria in biofilms than planktonic bacteria.[9] Reactive oxygen species (ROS) can disintegrate the extracellular polymeric matrix of biofilms, disrupt the bacterial cell membrane, and damage DNA, leading to the death of Gram-positive and Gram-negative antibiotic-resistant bacteria.[10,11] Glucose oxidase and horseradish peroxidase have been often employed in enzyme cascade catalysis to produce ROS from glucose and O_2, respectively.[12,13] However, natural enzymes, mostly proteins, may lose their catalytic activity in challenging environments such as the low pH inside biofilms.[14,15] The isolation of natural enzymes is difficult and costly, which limits its application.[16] To solve this problem, artificial nanozymes combining the unique properties of nanomaterials with the catalytic activities of natural enzymes need to be developed.[17,18]

Among various nanomaterials, two-dimensional (2D) nanosheets with a high surface area and defects for electron transport have been reported for their applications in photoinduction and photocatalysis to produce ROS.[19,20] The electronic structure of graphitic carbon nitride (g-C_3N_4) with graphitic planes formed by triazine units can provide a visible-light response. Therewith, g-C_3N_4 can be used as a photosensitizer for the generation of ROS, which can be used as an antimicrobial. Previous studies have shown the potential of g-C_3N_4 as a bifunctional nonenzymatic cascade for glucose and peroxide detection.[21,22] Nonetheless, limited by

Received: September 4, 2024
Revised: March 6, 2025
Accepted: March 6, 2025
Published: March 14, 2025

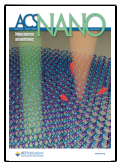

https://doi.org/10.1021/acsnano.4c12348
ACS Nano 2025, 19, 10816−10828

Scheme 1. Synthesis of Single-Atom Cu-g-C_3N_4/PCL Nanofibers and the Reaction Mechanism of Cu-*g*-C_3N_4 Nanosheets as Glucose Oxidase-Like and Peroxidase-Like with Light Irradiation or Dark Conditions to Eradicate Bacteria[a]

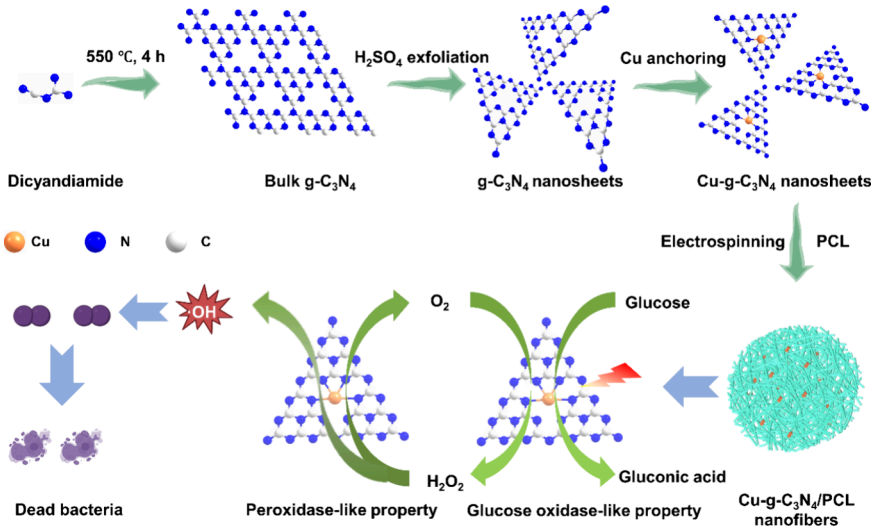

[a]The glucose oxidase-like Cu-*g*-C_3N_4 nanosheets oxidized glucose to generate gluconic acid and hydrogen peroxide (H_2O_2) in the presence of light and oxygen. The H_2O_2 generated *in situ* reacted with Cu-*g*-C_3N_4 as a peroxidase-like enzyme to format hydroxyl radicals (·OH) to kill bacteria.

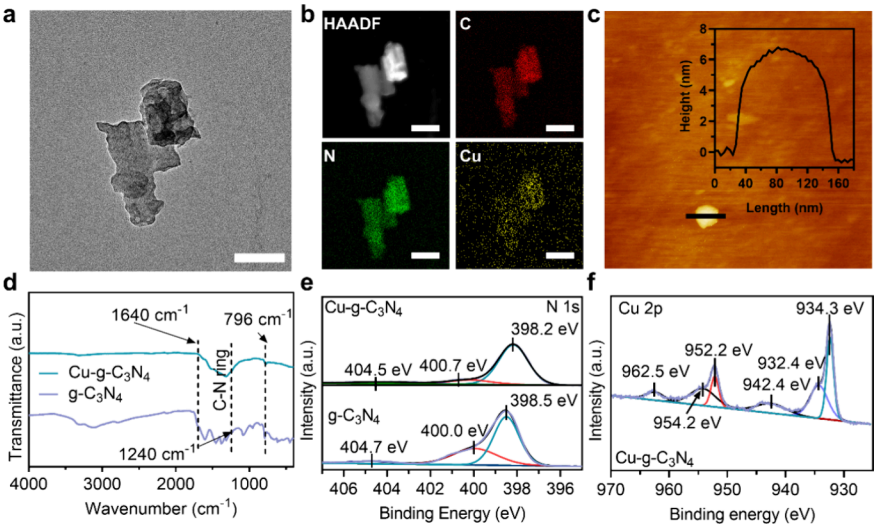

Figure 1. Structural characterizations of single-atom Cu-*g*-C_3N_4 nanosheets. (a) Transmission electron microscopy (TEM) image of Cu-*g*-C_3N_4 nanosheets. Scale bar = 100 nm. (b) High-angle annular dark-field (HAADF) of TEM images showing the distribution of C, N, and Cu. Scale bar = 100 nm. (c) Atomic force microscopy (AFM) image and a length and height profile of a Cu-*g*-C_3N_4 nanosheet. (d) Fourier transform infrared (FT-IR) spectra of g-C_3N_4 and Cu-*g*-C_3N_4 nanosheets. (e) X-ray photoelectron spectroscopic (XPS) narrow scan spectra of N 1s of g-C_3N_4 and Cu-*g*-C_3N_4 nanosheets. (f) XPS narrow scan Cu 2p from Cu-*g*-C_3N_4 nanosheets (Figure S4 shows a wide scan).

the low utilization efficiency of visible light, its therapeutic efficacy on bacterially infected wounds *in vivo* is not satisfying. Taking advantage of surface defects and topological insulation of nanosheets, which is enhancing electron transport, metal atoms have been added into these defects of the nanosheets to improve the enzymatic cascade efficiency.[21,23]

Here, we present a bifunctional nanozyme, a single-atom copper-anchored g-C_3N_4 nanosheet (Cu-*g*-C_3N_4). Cu-*g*-C_3N_4 plays a dual role in glucose oxidase-like or peroxidase-like activity in chromogenic substrate oxidation with visible-light irradiation or dark conditions, respectively, to accomplish a cascade reaction (Scheme 1). H_2O_2 produced *in situ* from glucose oxidation and dioxygen reduction was utilized for peroxidation of a chromogenic substrate on Cu-*g*-C_3N_4 nanosheets to obtain hydroxyl radicals showing broad-spectrum activity against different multidrug-resistant bacteria. The excellent enzyme activity of Cu-*g*-C_3N_4 compared to that of g-C_3N_4 and other metals (Cr, K, Fe, and Zn) anchored with g-C_3N_4 arises from its high light absorption ability and surface adsorption. Furthermore, Cu-*g*-C_3N_4 nanosheets with polycaprolactone (PCL) nanofibers were prepared via electrospinning as a wound dressing to evaluate Cu-*g*-C_3N_4 performances on bacterial infection control. Cu-*g*-C_3N_4/PCL, as a dressing, was then systematically investigated for antibacterial and anti-inflammatory activities, biocompatibility, and wound healing potential *in vitro* and *in vivo*. This work uniquely integrates single-atom nanozymes on nanofibers as a dressing that can be used in hospitals during surgery and for the clothing of nurses and doctors, broadening the design and application of nanozymes.

https://doi.org/10.1021/acsnano.4c12348
ACS Nano 2025, 19, 10816−10828

RESULTS

Synthesis and Characterizations of Cu-*g*-C_3N_4 Nanosheets. Density functional theory calculations revealed that Cu delivered the highest adsorption energy during adsorption to g-C_3N_4 compared to Fe, Cr, Zn, and K (Figure S1a). Cu-*g*-C_3N_4 had the highest light absorption (Figure S1b), and also Cu-*g*-C_3N_4 showed the highest antibacterial properties against *Staphylococcus aureus* Xen36 compared with Fe-*g*-C_3N_4, Cr-*g*-C_3N_4, K-*g*-C_3N_4, and Zn-*g*-C_3N_4 (Figure S1c,d). Therefore, Cu-*g*-C_3N_4 nanosheets were selected to investigate further. The synthesis and reaction mechanism of g-C_3N_4 and Cu-*g*-C_3N_4 nanosheets is illustrated in Scheme 1. Bulk g-C_3N_4 was synthesized and exfoliated by sulfuric acid to obtain g-C_3N_4 nanosheets (Figure S2). These nanosheets showed characteristic structures of g-C_3N_4 in X-ray powder diffraction spectra, with two characteristic diffraction peaks at 12.6 and 27.9°, corresponding to (100) and (002) planes,[24] respectively (Figure S3). Introduction of Cu into g-C_3N_4 nanosheets resulted in a decrease in the crystallinity of the nanosheets. However, no peaks assigned to Cu hydroxides or oxides were detected (Figure S3), indicating that Cu atoms did not form crystalline phases in g-C_3N_4, which was confirmed by TEM where no crystalline lattices were observed on Cu-*g*-C_3N_4 nanosheets (Figure 1a). EDS elemental mapping illustrated the distributions of carbon, nitrogen, and copper (Figure 1b). The size of the Cu-*g*-C_3N_4 nanosheets was measured with AFM and was 120 nm in length and 6−7 nm in height (Figure 1c).

Quantification by inductively coupled plasma optical emission spectrometry (ICP-OES) detected that 16.3 wt % of Cu was successfully anchored in g-C_3N_4 nanosheets. FT-IR peaks at 3310 and 3140 cm^{-1} indicated the stretching vibrations of ν_{O-H} and $\nu_{N-H,}$ respectively;[25,26] peaks at 1240−1640 cm^{-1} showed the presence of the C−N ring structure, and peaks at 796 cm^{-1} corresponded to the triazine structure of g-C_3N_4 (Figure 1d).[27] The local framework composition of g-C_3N_4 like the C-NH_x bonding structure (404.5 eV), bridging nitrogen atoms in N−$(C)_3$ (400.7 eV), and sp^2-hybridized nitrogen atoms in C═N−C (398.2 eV) remained in Cu-*g*-C_3N_4 nanosheets (Figure 1e).[28] Cu 2p XPS (Figure 1f) showed peaks at 934.3 and 954.2 eV, which are attributed to Cu $2p_{3/2}$ and Cu $2p_{1/2}$ of Cu^{2+},[29] respectively. The peaks at 942.8 and 962.5 eV, due to the empty 3d shell of Cu^{2+},[30] and the peaks at 932.4 and 952.2 eV are related to the presence of Cu $2p_{3/2}$ and Cu $2p_{1/2}$ of Cu^{+}.[31] In short, the structural skeleton of g-C_3N_4 was maintained, and Cu atoms were strongly integrated with g-C_3N_4 in the Cu-*g*-C_3N_4 nanosheets.

To further investigate the binding of Cu in g-C_3N_4 nanosheets at the atomic level, X-ray absorption near-edge structure (XANES) and extended X-ray absorption fine structure (EXAFS) spectroscopy at the Cu K-edge were conducted. Cu foil, CuO, and Cu phthalocyanine (Cu-Pc) were chosen as reference materials for Cu−Cu, Cu−O, and Cu−N coordination materials, respectively. From Cu K-edge XANES spectra (Figure 2a), the absorption edge of Cu-*g*-C_3N_4 was positioned between the Cu foil and CuO, indicating that the oxidation valence state of the Cu atom was higher than that of metallic Cu^0 and lower than that of Cu^{2+}. The spectrum of Cu-*g*-C_3N_4 was very similar to Cu-Pc, indicating that the coordination of Cu atoms in Cu-*g*-C_3N_4 was Cu−N. For Fourier transform EXAFS spectra (Figure 2b), the curve of Cu-*g*-C_3N_4 nanosheets showed a clear peak at 1.4 Å, which is close

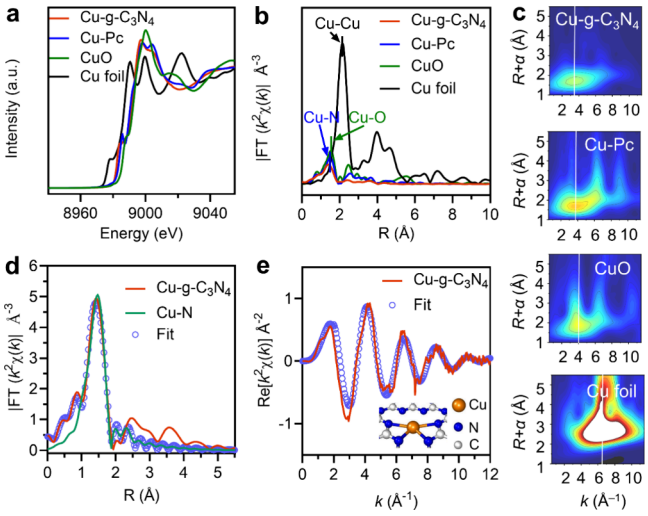

Figure 2. Atomic structural analysis of Cu-*g*-C_3N_4 nanosheets. (a) Cu K-edge XANES spectra of Cu-*g*-C_3N_4, copper phthalocyanine (Cu-Pc), CuO, and Cu foil. (b) k^3-weighted Fourier-transformed (FT) spectra from extended X-ray absorption fine structure (EXAFS) of Cu-*g*-C_3N_4, Cu-Pc, CuO, and Cu foil. (c) Wavelet transform (WT) of the k^3-weighted EXAFS for Cu-*g*-C_3N_4, Cu-Pc, CuO, and Cu foil. The white line is the *k*-value. (d) Fit of the Cu-*g*-C_3N_4 EXAFS spectrum in R space. (e) Fit of the Cu-*g*-C_3N_4 EXAFS spectrum in *k*-space; the inset shows the corresponding model structure.

to the single atomically dispersed Cu agents.[32] No Cu−Cu coordination peak around 2.2 Å was observed in the Cu-*g*-C_3N_4 nanosheets, suggesting that all copper species exist as isolated single atoms. The wavelet transformation (Figure 2c) showed that the peak of Cu-*g*-C_3N_4 nanosheets tends to have a lower *k* value than that of CuO and Cu foil and is close to Cu-Pc, further confirming that Cu−Cu bonds were not present in Cu-*g*-C_3N_4 nanosheets and the Cu−N bond exists in Cu-*g*-C_3N_4 nanosheets. Quantitative EXAFS curve fitting analysis (Figure 2d,e and Table S1) was performed to investigate the structural parameters of Cu-*g*-C_3N_4. The Cu−N coordination number is ∼4.2, meaning that the isolated Cu atom is fourfold coordinated by N atoms (Figure 2e, inset). The calculated Cu−N_4 mean bond distance in Cu-*g*-C_3N_4 is 1.92 Å. Summarizing, the Cu is single atomically anchored in g-C_3N_4 nanosheets to form single-atom Cu-*g*-C_3N_4 nanosheets.

Glucose Oxidation and Peroxidase Cascade Catalytic Reactions. The mechanism of cascade enzymes' sequential catalysis is illustrated in Scheme 1. The concentration of H_2O_2 was detected by the *N*,*N*-diethyl-1,4-phenylenediamine (DPD) and peroxidase by measuring the absorbance at 551 nm (Figure 3a). Cu-*g*-C_3N_4 nanosheets showed a higher glucose oxidase activity than g-C_3N_4 nanosheets (Figure S5), which is attributed to its increased light absorption capacity due to the Cu atom enhancing electron transportation (Figure S1a,b). The H_2O_2 concentration generated from glucose oxidation was calculated using eq 1:

$$[M] = \mathrm{Abs}/l\varepsilon \quad (1)$$

in which $[M]$ is the product (H_2O_2) concentration, Abs is the UV−vis absorbance of $DPHD^{\bullet+}$ at 551 nm, l = 1 cm, and ε = 21,000 M^{-1} cm^{-1}.

The generation of H_2O_2 was 4.7 × 10^{-6}, 8.1 × 10^{-6}, 11 × 10^{-6}, and 15 × 10^{-6} M from glucose concentrations of 1, 2, 4,

https://doi.org/10.1021/acsnano.4c12348
ACS Nano 2025, 19, 10816−10828

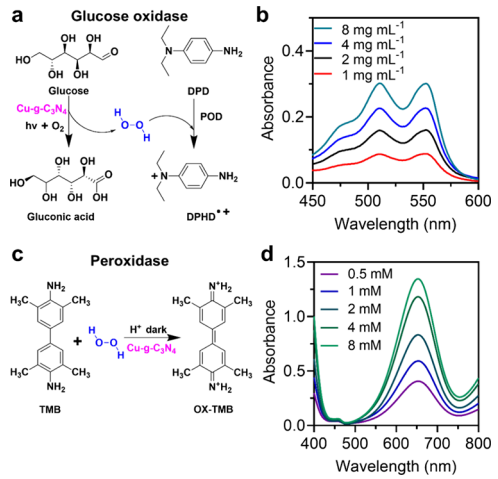

Figure 3. Glucose oxidase and peroxidase activities of single-atom Cu-*g*-C_3N_4 nanosheets. (a) Scheme of glucose oxidase-like reactions of Cu-*g*-C_3N_4 nanosheets. (b) UV−vis spectra of H_2O_2 generation from different glucose concentrations with Cu-*g*-C_3N_4 nanosheets (50 μg mL^{-1}) in phosphate buffer (pH 7) and visible-light irradiation for 30 min ($\lambda \geq 420$ nm, 0.2 W cm^{-1}) using *N*,*N*-diethyl-l,4-phenylenediammonium sulfate (DPD) and peroxidase (POD). (c) Scheme of peroxidase-like reaction. (d) UV−vis spectra of Cu-*g*-C_3N_4 nanosheets for different H_2O_2 concentrations as the substrate in acetate buffer (0.1 M, pH 4) after 10 min incubation. The baseline in (b) and (d) have been corrected.

and 8 mg mL^{-1}, respectively, which shows that the yields were dependent on the glucose concentration (Figure 3b).

The intrinsic peroxidase-like activity of Cu-*g*-C_3N_4 nanosheets was determined by the oxidation of TMB (3,3′,5,5′-tetramethylbenzidine) (Figure 3c). OX-TMB generated from TMB and H_2O_2 was calculated using eq 1 with different parameters: $[M]$ is the OX-TMB concentration generated from H_2O_2 and TMB, Abs is the UV−vis absorbance of OX-TMB at 652 nm, l = 1 cm, and ε = 39,000 M^{-1} cm^{-1}. The OX-TMB concentrations were 1.0 × 10^{-5}, 1.5 × 10^{-5}, 2.1 × 10^{-5}, 3.5 × 10^{-5}, and 3.5 × 10^{-5} M from different H_2O_2 concentrations of 0.5, 1, 2, 4, and 8 mM, respectively. The yields of OX-TMB were dependent on the concentration of H_2O_2 (Figure 3d). The ·OH generated from the cascade reaction was detected by terephthalic acid, which confirmed ·OH generation after exposure to Cu-*g*-C_3N_4 (Figure S6). The above results show that the single-atom Cu-*g*-C_3N_4 nanosheet is an effective nanozyme to initialize the cascade reaction of glucose oxidation and H_2O_2 reduction.

Density Functional Theory Calculations. Strong binding of metal atoms on the substrate is mandatory for their catalytic activities and long-term uses.[33] In Figure 4a, electron properties near the Fermi level (E_f) obtained from Cu-*g*-C_3N_4 nanosheets were analyzed using the density of their energy states. A large overlap between N and Cu orbitals was observed, confirming a tight electron interaction between Cu and N, which is required for the strong anchoring of Cu single atoms on g-C_3N_4 nanosheets.

Strong adsorption of O_2 and H_2O_2 on the surface of Cu-*g*-C_3N_4 nanosheets is crucial for the reaction efficiency (Scheme 1). The adsorption energies were calculated, and the corresponding structural configurations of each intermediate on g-C_3N_4 and Cu-*g*-C_3N_4 nanosheets showed different locations for the oxygen species in Figure 4c,d and Figure S7. The adsorption energy of O_2 on Cu-*g*-C_3N_4 nanosheets (−2.29 eV) calculated using eq 2 was lower than on g-C_3N_4 nanosheets (0.40 eV), and also the adsorption energy of H_2O_2 onto Cu-*g*-C_3N_4 nanosheets (−2.77 eV) was lower than for g-C_3N_4 nanosheets (−2.34 eV). The lower adsorption energy caused a higher activity of glucose oxidase and peroxidase

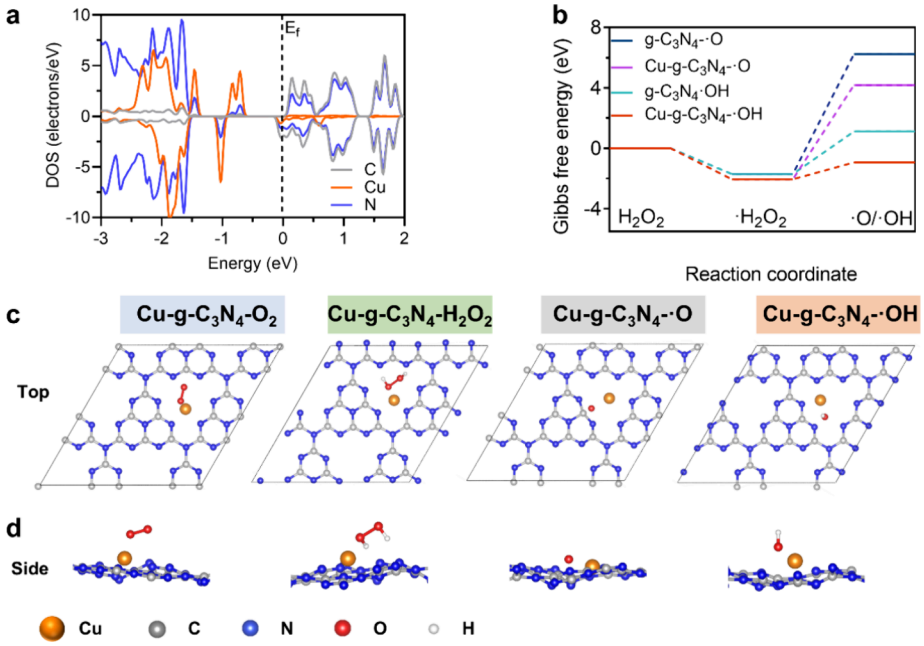

Figure 4. Density functional theory calculations on g-C_3N_4 and single-atom Cu-*g*-C_3N_4 nanosheets. (a) Density of electron states (DOS) and orbital distribution of the elements C, N, and Cu in Cu-*g*-C_3N_4 nanosheets; E_f is the Fermi level. (b) Gibbs free energy (ΔG) diagrams of ·O or ·OH on g-C_3N_4 and Cu-*g*-C_3N_4. Before the generation of ·O and ·OH, an intermediate ·H_2O_2 is formed due to the decomposition of H_2O_2 on the nanosheet's surface. The reaction energy is calculated from H_2O_2 to ·H_2O_2, and then to ·O or ·OH. (c) Top view of the optimized structure of O_2, H_2O_2, ·O, and ·OH on Cu-*g*-C_3N_4 nanosheets and (d) same as (c), which is the side view.

https://doi.org/10.1021/acsnano.4c12348
ACS Nano 2025, 19, 10816−10828

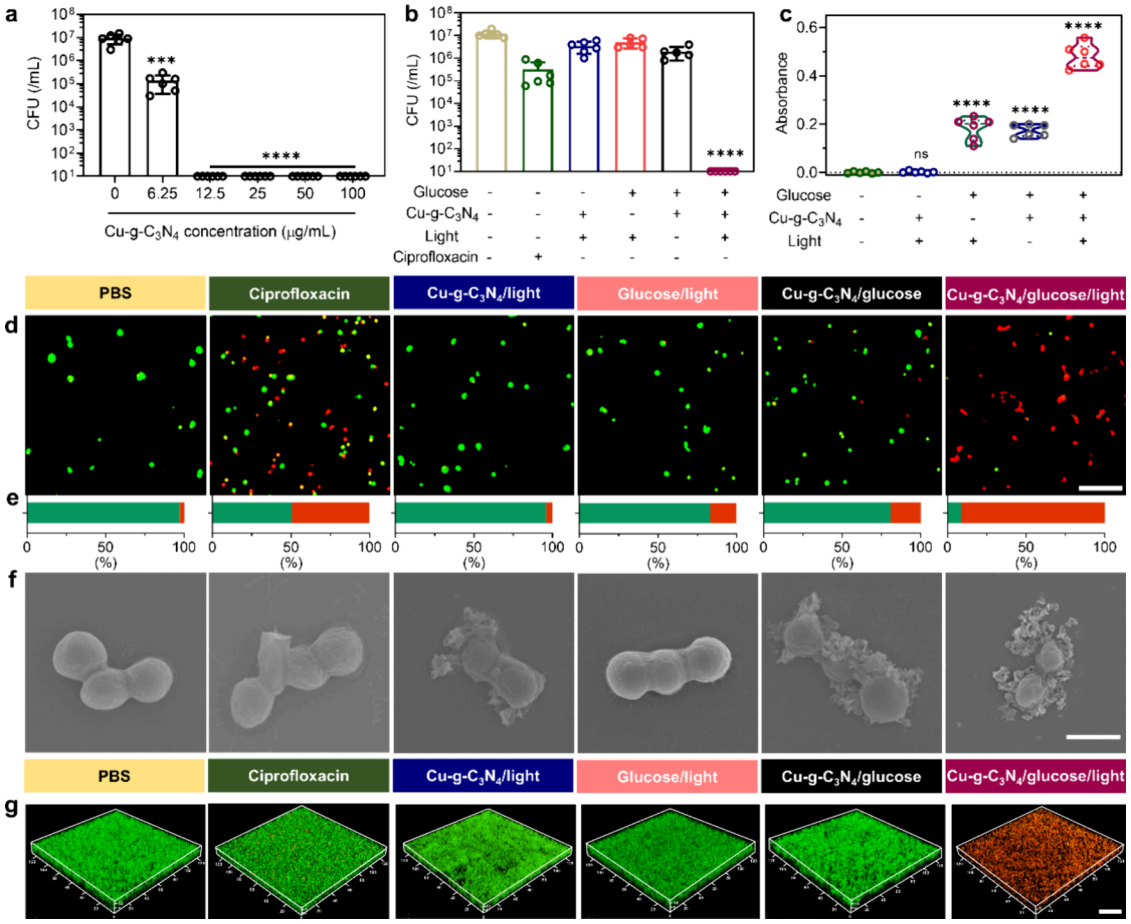

Figure 5. Killing efficacy of single-atom Cu-*g*-C_3N_4 nanosheets *in vitro* on planktonic *S. aureus* Xen36 and 24 h old biofilms exposed to Cu-*g*-C_3N_4 with or without glucose and light irradiation. (a) Killing efficacy on planktonic bacteria (10^7 bacteria mL^{-1}) of different concentrations of Cu-*g*-C_3N_4 nanosheets (glucose concentration: 4 mg mL^{-1}, light irradiation: $\lambda \geq 420$ nm, 0.2 W cm^{-1}, 30 min). (b) Killing efficacy on planktonic bacteria (10^7 bacteria m^{-1}) of Cu-*g*-C_3N_4 nanosheets (12.5 μg mL^{-1}) with or without the presence of glucose (4 mg mL^{-1}) or light irradiation, PBS, and ciprofloxacin (12.5 μg mL^{-1}) as controls. (c) Absorbance of the protein release after exposure to Cu-*g*-C_3N_4 with and without glucose and light irradiation of planktonic *S. aureus* Xen36 measured by using the BCA kit. (d, e) CLSM images and quantification of live/dead staining after 20 min exposure to PBS, ciprofloxacin (12.5 μg mL^{-1}), and Cu-*g*-C_3N_4 nanosheets of planktonic *S. aureus* Xen36 (10^7 bacteria mL; Cu-*g*-C_3N_4 nanosheets: 12.5 μg mL^{-1}; glucose: 4 mg mL^{-1}; light irradiation, scale bar is 10 μm. (f) FESEM images of planktonic *S. aureus* Xen36 after different exposures, scale bar is 1 μm. (g) CLSM images of 48 h old biofilms of *S. aureus* Xen36 after different exposures to Cu-*g*-C_3N_4 nanosheets and PBS and ciprofloxacin as controls and stained with live/dead stain; scale bar is 20 μm. Green fluorescent represents live bacteria stained by SYTO 9, and red represents membrane-damaged bacteria stained by propidium iodide. Statistical significance of differences with respect to PBS exposure ($n = 6$) indicates as ***$p < 0.001$ and ****$p < 0.0001$, and ns stands for no significant difference.

activity for the Cu-*g*-C_3N_4 nanosheets. For the formation of •OH from H_2O_2, the first step is the decomposition of H_2O_2 to form $\cdot H_2O_2$, and the corresponding reaction energy is −2.05 eV for Cu-*g*-C_3N_4 and −1.77 for g-C_3N_4 nanosheets (Figure 4b and Table S2). The second step is the generation of •OH from $\cdot H_2O_2$ by using g-C_3N_4 and Cu-*g*-C_3N_4 nanosheets. Decomposition of $\cdot H_2O_2$ into water and the free oxygen radical ($\cdot H_2O_2 \rightarrow H_2O + \cdot O$) resulted in a reaction energy of 6.23 eV, higher than the energy for the generation of •OH (1.11 eV). Clearly, Cu-*g*-C_3N_4 showed a lower reaction energy for $\cdot H_2O_2$ and •OH generation, making Cu-*g*-C_3N_4 nanosheets an efficient catalyst for H_2O_2 conversion.

Antibacterial and Antibiofilm Activities. The antibacterial and antibiofilm activity of Cu-*g*-C_3N_4 nanosheets was evaluated *in vitro* for *S. aureus*, one of the most common bacteria causing wound infections (Figure 5). The optimal concentration of Cu-*g*-C_3N_4 nanosheets for killing all planktonic *S. aureus* Xen36 was 12.5 μg mL^{-1} (Figure 5a), which was used in all of the following experiments. Only Cu-*g*-C_3N_4 in the presence of glucose and light irradiation achieved antibacterial activity, which proves that the antibacterial activity of Cu-*g*-C_3N_4 nanosheets was due to the cascade reaction of glucose oxidation and H_2O_2 reduction (Figure 5b). This conclusion is supported by the CLSM micrographs shown in Figure 5d and Figure 5e, where 90% of bacteria were dead (cell membrane damaged) after exposure to Cu-*g*-C_3N_4/glucose/light. This was much higher than that of the bacteria exposed to Cu-*g*-C_3N_4 and glucose without light irradiation, where only 20% of bacteria were dead. Ciprofloxacin was used for comparison of the antibacterial activity of the Cu-*g*-C_3N_4/glucose/light treatment. The killing efficiency of ciprofloxacin against the drug-resistant *S. aureus* Xen36 was lower (50%) than the exposure to Cu-*g*-C_3N_4/glucose/light nanosheets. Field-emission scanning electron microscopy (FESEM) showed that Cu-*g*-C_3N_4 nanosheets aggregated around bacteria, leading to shrinkage of the bacteria when glucose

https://doi.org/10.1021/acsnano.4c12348
ACS Nano 2025, 19, 10816−10828

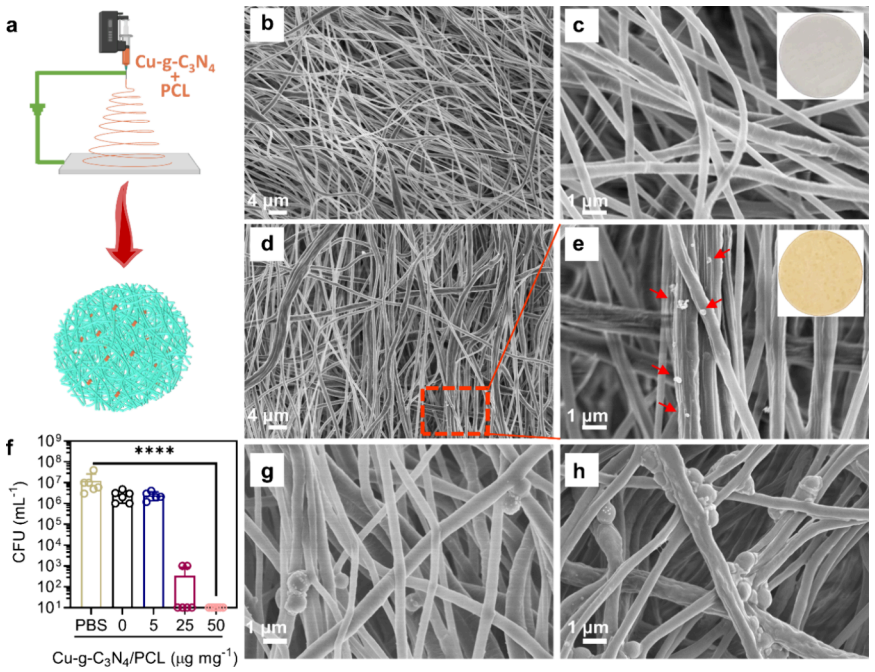

Figure 6. Synthesis of Cu-*g*-C_3N_4/PCL nanofibers and their antibacterial activity *in vitro*. (a) Schematic synthesis process of Cu-*g*-C_3N_4/PCL nanofibers. (b, c) FESEM of PCL nanofibers and inset in (c) is a piece of the PCL nanofiber. (d, e) FESEM of Cu-*g*-C_3N_4/PCL nanofibers and inset in (e) is a piece of Cu-*g*-C_3N_4/PCL nanofiber (red arrows are the Cu-*g*-C_3N_4 nanosheets). (f) Killing efficacy of Cu-*g*-C_3N_4/PCL nanofibers with different concentrations of Cu-*g*-C_3N_4 in the nanofibers in the presence of glucose and light irradiation of *S. aureus* Xen36 (2×10^7 mL^{-1} in PBS, pH 7.4. Weight of nanofibers: 100 mg; glucose: 4 mg mL^{-1}; light: $\lambda \geq 420$ nm, 0.2 W cm^{-2}, 30 min). (g) FESEM image of *S. aureus* Xen36 on PCL nanofibers and (h) the same as (g) but now on Cu-*g*-C_3N_4/PCL nanofibers with glucose and light for 30 min. Error bars indicate means ± SD ($n = 6$), ****$p < 0.0001$.

and light were used (Figure 5f). Only bacteria exposed to Cu-*g*-C_3N_4/glucose/light demonstrated completely collapsed bacterial cell walls, which could be due to the ROS disruption of these cell walls. This result is consistent with the findings of the leakage of proteins from bacteria (Figure 5c), where Cu-*g*-C_3N_4/glucose/light treatment significantly increased the permeability of bacterial cell walls, leading to the leakage of bacterial cytoplasm (Figure 5c). Moreover, Cu-*g*-C_3N_4/glucose/light effectively damaged the cell walls of *S. aureus* Xen36 biofilms (Figure 5g), where only red staining was observed. The antibacterial activity of Cu-*g*-C_3N_4 was also evaluated against various multidrug-resistant bacteria, and broad-spectrum antibacterial activity was demonstrated regardless of Gram-positive or Gram-negative bacteria (Figure S8). Cytotoxicity results showed no toxicity to fibroblasts (L929 cells) after being incubated with Cu-*g*-C_3N_4 (12.5 μg mL^{-1}) for 24 h (Figure S9). Summarizing, only Cu-*g*-C_3N_4 nanosheets irradiated with light in the presence of glucose achieved effective bacterial killing in their planktonic and biofilm modes of growth, indicating that Cu-*g*-C_3N_4 nanosheets are effective light-induced glucose oxidase-like and peroxidase-like enzymes involved in ROS generation.

Synthesis of Cu-*g*-C_3N_4/PCL Nanofibers and Their Antibacterial Activity *In Vitro*. To apply Cu-*g*-C_3N_4 in a wound dressing, Cu-*g*-C_3N_4/PCL nanofibers were loaded with Cu-*g*-C_3N_4 onto PCL nanofibers with electrospinning technology (Figure 6a). PCL was used as the material for the nanofibers to prepare the wound dressing because it is a hydrophobic material that can be easily removed from the wound after treatment. In contrast to the smooth surface of pure PCL nanofibers (Figure 6b,c), Cu-*g*-C_3N_4/PCL nanofibers possessed a rough surface covered with Cu-*g*-C_3N_4/PCL (Figure 6d,e). The successfully synthesized Cu-*g*-C_3N_4/PCL nanofibers killed planktonic *S. aureus* Xen36 most effectively at a concentration of 50 μg mg^{-1} in the presence of glucose and light irradiation (Figure 6f). Bacterial morphology remains intact on PCL nanofibers (Figure 6g), but it is damaged on Cu-*g*-C_3N_4/PCL nanofibers (Figure 6h). The Cu-*g*-C_3N_4/PCL nanofibers showed zone of inhibitions for *S. aureus* Xen36 at a concentration of 25 μg mg^{-1} or higher (Figure S10). These findings provide evidence that Cu-*g*-C_3N_4/PCL nanofibers can be used as an antibacterial wound dressing *in vivo*.

Cu-*g*-C_3N_4/PCL Nanofiber Wound Dressing for an Infectious Biofilm in a Skin Wound in a Mouse Model. Cu-*g*-C_3N_4/PCL nanofibers were prepared as wound dressings to treat bacterial infections in an open-wound infection model.[10] The animal experimental design is illustrated in Figure 7a. From the images and quantification of wound areas (Figure 7b and Figure S11), wounds treated with Cu-*g*-C_3N_4/PCL/glucose/light cured faster than those treated with the other treatments. The bioluminescence intensity of *S. aureus* Xen36 bacteria decreased with time and disappeared after 2 days in mice treated with Cu-*g*-C_3N_4/PCL nanofibers in the presence of glucose and light (Figure 7c,d). Note that the low bioluminescence signal measured after day 2 is background bioluminescence (Figure 7d). CFU counts per milligram of tissue were significantly lower compared to PBS in wounds with Cu-*g*-C_3N_4/PCL/glucose/light treatment (Figure 7e). Treatment of the wound infected with *S. aureus* Xen36 with the antibiotic ciprofloxacin demonstrated a much slower wound healing than treatment with Cu-*g*-C_3N_4/PCL/glucose/light (Figure 7).

To evaluate the inflammatory process of the early phase on day 2 of wound healing, wound tissues were collected.

https://doi.org/10.1021/acsnano.4c12348
ACS Nano 2025, 19, 10816−10828

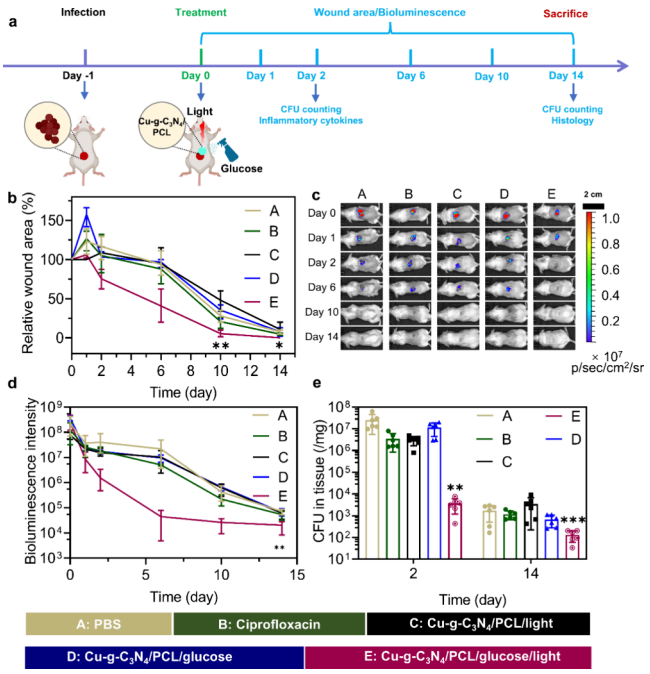

Figure 7. Cu-*g*-C_3N_4/PCL nanofibers as a wound dressing to treat *S. aureus* Xen36 biofilm infection *in vivo*. (a) Diagram of the animal experimental design of Cu-*g*-C_3N_4/PCL nanofibers as wound dressings for bacterial infection in the presence or absence of glucose (10 μL, 4 mg mL^{-1}) and light irradiation for 30 min ($\lambda \geq 420$ nm, 0.2 W cm^{-1}). The PBS and ciprofloxacin (10 μL, 12.5 μg/mL) were used as the control groups. (b) Relative wound area with different treatments on days 0, 1, 2, 6, 10, and 14 calculated with ImageJ from Figure S11. (c) Bioluminescence images of mice with different treatments on days 0, 1, 2, 6, 10 and 14. (d) Bioluminescence intensity obtained from (c). (e) CFU counts of bacteria on days 2 and 14 in the wound tissue. Asterisks indicate statistically significant differences to the PBS treatment *$p < 0.05$, **$p < 0.01$, and ***$p < 0.001$.

Hematoxylin and eosin (H&E) and Masson tissue staining were performed on day 6. Wound sites treated with Cu-*g*-C_3N_4/PCL/glucose/light showed intact, multilayer epidermis with abundant, newly regenerated hair follicles and very few inflammatory cells (Figure S12a), as well as ample, orderly arranged collagen and vascular structures (Figure S12b), which indicates wound healing. On day 2, the expression of pro-inflammatory cytokines was measured. IL-1β, IL-6, and TNF-α decreased, and anti-inflammatory cytokine, IL-10, increased when the infected wound was exposed to Cu-*g*-C_3N_4/PCL/light/glucose nanofibers (Figure S12c–f). Histological analysis of mice's major organs (heart, liver, spleen, lung, and kidney) after being treated with Cu-*g*-C_3N_4/PCL (Figure S13) for 14 days did not show abnormalities, which indicates that the Cu-*g*-C_3N_4/PCL nanofibers are biosafe and can be used as wound dressing material.

DISCUSSION

The emergence of catalytic nanozymes that emulate the functionalities of natural enzymes holds immense promise as potential agents for combating bacterial infections.[15,16] Here, we first synthesized g-C_3N_4 nanosheets from bulk g-C_3N_4 and then introduced Cu to prepare a single-atom Cu-*g*-C_3N_4 nanozyme. The single-atom Cu-*g*-C_3N_4 nanozyme exhibits dual-glucose oxidase-like and peroxidase-like activities, orchestrating a cascade reaction that leads to the generation of targeted ·OH (Scheme 1). In contrast to other cascade reaction devices utilizing extra commercial glucose oxidase,[34−37] the Cu-*g*-C_3N_4 nanozyme possesses its own glucose oxidase-like activity, thereby reducing costs. On the other hand, directly injecting H_2O_2 into the human body is, in general, not desirable. In our study, the addition of H_2O_2 is not necessary since H_2O_2 is generated from naturally occurring glucose, which reduces the potential harm to the tissue. The Cu-*g*-C_3N_4 nanozyme showed to eradicate planktonic bacteria and biofilms in a low concentration (12.5 μg mL^{-1}) with adequate biosafety (Figures S9 and S13), providing the potential of this nanozyme as a promising strategy for combating bacterial infections through innovative enzymatic mimicking.

A notable highlight of our study is the identification of Cu-*g*-C_3N_4 as a single-atom nanozyme (Figure 2). The promising attribution of single-atom nanozymes has been well recognized, offering a novel avenue for enhanced enzymatic catalysis.[38,39] Our results provide evidence that Cu outperforms other metals when anchored with g-C_3N_4, emphasizing its superior efficacy in this context (Figure S1). Cu-*g*-C_3N_4, as a single-atom nanozyme, enhances the generation of ·OH because of the strong adsorption of O_2 and H_2O_2 molecules, which increases enzymatic catalysis. Carbon nitride nanozymes as bifunctional glucose oxidase-peroxidase have been used in solutions to generate ROS.[21,40,41] In this study, we found that carbon nitride anchored with single-atom Cu can be used against planktonic multidrug-resistant bacteria (Figure S8) but also kill biofilm bacteria (Figure 5). By unveiling the potential of single-atom nanozymes such as Cu-*g*-C_3N_4, our work lays the foundation for a new frontier in the exploration of single-atom nanozymes within the enzymatic catalysis domain and broader biomedicine applications, offering promising avenues for transformative advancements in various scientific and practical arenas.

Cu-*g*-C_3N_4 nanosheets were introduced in the PCL nanofibers by electrospinning to obtain a wound dressing that can be applied on infected wounds (Figure 7). Although the control experiments showed that a wound is also healing due to the host defense system, Cu-*g*-C_3N_4/PCL nanofibers with the addition of glucose and light irradiation accelerate the healing rate by a factor of 5 even when compared to ciprofloxacin. Except for the eradication of bacteria, inflammatory cells migrate to the wound site to clear debris and pathogens (Figure S12). Subsequently, fibroblasts produce collagen, while angiogenesis occurs to establish new blood vessels, providing structural support and nourishment to the healing tissue.[42] Pro-inflammatory factors, including cytokines such as IL-1β, IL-6, and TNF-α, orchestrate the immune response and stimulate tissue repair mechanisms. Concurrently, anti-inflammatory cytokines such as IL-10 help regulate inflammation and promote tissue remodeling. Both bacterial eradication and inflammatory response are required to accelerate infected wound healing.

Small quantities of electrospun nanofibers are necessary for biomedical and healthcare applications, which makes them very attractive for wound dressings, implants, drug delivery devices, and *in vitro* disease platforms.[43,44] Therefore, if different functions could be developed and integrated into textiles, then Cu-*g*-C_3N_4/PCL nanofibers would increase opportunities to infiltrate them in human daily life. Nanofibers can be explored and utilized in the development of textiles for

https://doi.org/10.1021/acsnano.4c12348
ACS Nano 2025, 19, 10816−10828

use in hospitals during surgery, as well as for the clothing of nurses and doctors.

STUDY LIMITATIONS

Whereas this study successfully describes the antibacterial activity of single-atom Cu-*g*-C_3N_4/PCL/glucose/light, it is not investigated whether the concentration of glucose in the patient is enough or extra glucose needs to be added. The concentration of glucose for healthy human fasting blood is 0.6−0.99 mg mL^{-1}, and that for diabetic patients is higher than 1.26 mg mL^{-1}.[45,46] For mice, the concentration range of glucose in blood is 0.7−1.2 mg mL^{-1}, depending on strain and conditions.[47] In our study, we added 4 mg mL^{-1} glucose when treating the wound, which is higher than available in humans and mice. Therefore, it is unclear whether it still works in patients without additional glucose using our material systems. Another challenge will be to reach the contact area between the wound and nanofibers with light irradiation. Probably a sheet instead of fibers prepared from Cu-*g*-C_3N_4/PCL will have better contact and can use the available glucose, but this needs further investigation. For broader applicability, it will be interesting to mix the nanofibers with textiles, but further investigation is also required on the ratio of the different fibers and the antibacterial activity.

CONCLUSIONS

In conclusion, a novel nanozyme is introduced based on single-atom Cu-anchored g-C_3N_4 nanosheets with demonstrable bifunctional enzyme-mimicking activity of glucose oxidase and peroxidase. With the intrinsic glucose oxidase activity, the H_2O_2 generated from photoreaction of oxygen and glucose *in situ* triggers the subsequent peroxidase activity. This bifunctional Cu-*g*-C_3N_4 nanozyme showed broad-spectrum antibacterial activity against various multidrug-resistant bacteria in both planktonic and biofilm modes of growth. Subsequently, the Cu-*g*-C_3N_4 nanozyme is successfully incorporated in PCL fibers by electrospinning as a wound dressing material, which maintains the antibacterial capacity of Cu-*g*-C_3N_4 and serves as an ideal carrier of Cu-*g*-C_3N_4 nanozyme for *in vivo* applications. In the *in vivo* infection model, Cu-*g*-C_3N_4/PCL nanofibers in the presence of light irradiation and glucose promote faster wound healing, which is attributed to a synergy of antibacterial effects and inflammatory relief. It can be a promising wound dressing material to prevent bacterial infections and result in a faster recovery of the wound compared with the antibiotic ciprofloxacin.

EXPERIMENTAL SECTION

Chemicals and Materials. Dicyandiamide, sulfuric acid (H_2SO_4), $Cu(NO_3)_2{\cdot}H_2O$, $Cr(NO_3)_2{\cdot}9H_2O$, $FeSO_4{\cdot}7H_2O$, $Zn(NO_3)_2{\cdot}6H_2O$, KCl, 3,3′,5,5′-tetramethylbenzidine (TMB), *N*,*N*-diethyl-1,4-phenylenediamine (DPD), sodium acetate, acetic acid, horseradish peroxidase, 4% paraformaldehyde fixation solution, glucose, terephthalic acid (TA), ciprofloxacin, and 5,5-dimethyl-1-pyrroline *N*-oxide (DMPO) were purchased from Macklin (Shanghai, China). H_2O_2 (30%) and absolute ethanol were obtained from Sigma-Aldrich (Shanghai, China). Sterile phosphate-buffered saline (PBS; 5 mM K_2HPO_4, 5 mM KH_2PO_4, and 150 mM NaCl, pH 7) was homemade and used in this study. Live/dead bacterial staining kit (SYTO 9, propidium iodide) was provided by Invitrogen (Shanghai, China). 0.25% trypsin/EDTA, agar powder (molecular weight, MW, 3000−9000), and BCA protein quantification kit were purchased from Solarbio (Beijing, China).

Synthesis of Bulk g-C_3N_4, g-C_3N_4 Nanosheets, and Cu-*g*-C_3N_4 Nanosheets. A thermal polymerization method was used to prepare bulk g-C_3N_4, as previously described.[48] Briefly, 6 g of dicyandiamide was added into a porcelain calcination boat and then heated from 20 to 550 °C within 4 h and kept at 550 °C for 4 h in air. After that, the bulk g-C_3N_4 were cooled to room temperature.

The g-C_3N_4 nanosheets were synthesized by dispersing 1 g of bulk g-C_3N_4 in 10 mL of H_2SO_4 (anhydrous) while stirring for 1 h. Subsequently, 10 mL of deionized water was dropped in the g-C_3N_4/H_2SO_4 solution until it turned from turbid to clear. The solution was added to 30 mL of absolute ethanol and stirred for 18 h, and the nanosheets were precipitated from the solution. Finally, the nanosheet suspension was dialyzed (membrane cutoff: 3500 kDa) in deionized water, which was refreshed every 3 h to remove both residual SO_4^{2-} and ethanol until its pH was 7.0, determined by pH paper. The g-C_3N_4 nanosheets were harvested by centrifugation at 5000*g* for 5 min and dried at 60 °C for 18 h.

The Cu-*g*-C_3N_4 nanosheets were synthesized by adding 2.0 g of g-C_3N_4 nanosheets and 0.65 g of $Cu(NO_3)_2{\cdot}H_2O$ into 10 mL of deionized water while stirring for 2 h. After drying on a hot plate (HP-05, Shanghai Xuesen Instrument Technology Co., Ltd.) for 8 h, the obtained powder was added in a semiclosed porcelain boat with a cover. It was heated in a tube furnace from room temperature to 130 °C with a heating rate of 10 °C min^{-1} under Ar flow and kept at this temperature for 9 h. After this step, the nanosheets were heated to 550 °C with a heating rate of 9 °C min^{-1} and kept at this temperature for 1 h. Then, the suspension with the Cu-*g*-C_3N_4 nanosheets was cooled down to room temperature, transferred to a 50 mL tube, washed five times with 30 mL of deionized water, and centrifuged at 5000*g* for 5 min. Finally, the sample was fully dried in a vacuum chamber at 60 °C for 18 h to obtain the powder of the nanosheets.

Synthesis of Cu-*g*-C_3N_4/PCL Nanofibers for Wound Dressing. The Cu-*g*-C_3N_4/PCL nanofibers were prepared by electrospinning. First, dichloromethane (4 mL) and *N*,*N*-dimethylformamide (1 mL) were mixed by stirring for 10 min, and then 25 mg of Cu-*g*-C_3N_4 powder was dispersed in the mixed solution and continuously stirred for another 1.5 h. Then, 250 mg of PCL was added into the Cu-*g*-C_3N_4 suspension and mixed by shaking overnight. The solution was diluted by *N*,*N*-dimethylformamide containing 10% PCL to the following mass ratio of Cu-*g*-C_3N_4/PCL, 50, 25, and 5 $\mu g\ mg^{-1}$. A 2 mL solution of each suspension was used for electrospinning. The parameters for electrospinning were electrical field strength 18 kV, flow rate of the solution 0.7 mL h^{-1}, and DC voltage 18 kV. Electrospinning was stopped when the liquid was fully used, and the collected nanofibers were carefully cut with a scalpel. All of the nanofibers were placed in a vacuum at 25 °C for 24 h to remove the residual solvent. The morphologies of nanofibers were studied by field-emission scanning electron microscopy (FESEM, HITACHI, SU8010, Japan).

Characterizations. X-ray powder diffraction (XRD, Bruker, D8 Advance, Germany) was employed to study the crystalline structure of g-C_3N_4 and Cu-*g*-C_3N_4 nanosheets with Cu Kα radiation at 40 kV and 40 mA. The morphologies and high-angle annular dark-field (HAADF) of as-prepared g-C_3N_4 bulk, g-C_3N_4 nanosheets, and Cu-*g*-C_3N_4 nanosheets were performed by transmission electron microscopy (TEM, FEI, F200S, USA). The functional groups were determined by a Fourier transform infrared spectrometer (Bruker, TENSOR II, Germany). The nanosheets were mixed with KBr and pressed in a tablet, and a blank KBr tablet was used as the background. Scans were recorded over the wavenumber range from 400 to 4000 cm^{-1} with a resolution of 0.4 cm^{-1}, and 16 scans were made and averaged. The height of the samples was measured by an atomic force microscope (AFM, Bruker, WM2017014, USA) with a silicon tip (height 8−20 μm, opening angle of ca. 30−40°, apex radius 10 nm). A UV−vis spectrophotometer (UV-2700, Agilent, Cary 5000, USA) was used at a wavelength range of 320−800 nm for determining the light absorption ability of g-C_3N_4, Cr-*g*-C_3N_4, Zn-*g*-C_3N_4, Fe-*g*-C_3N_4, K-*g*-C_3N_4, and Cu-*g*-C_3N_4 nanosheets. X-ray photoelectron spectroscopy (XPS, Kratos Analytical Ltd., Axis Ultra DLD, Germany) was used to analyze the elemental surface composition.

https://doi.org/10.1021/acsnano.4c12348
ACS Nano 2025, 19, 10816−10828

X-ray production was from Al-coated anodes using a spot size of 400 μm. Wide scans were over the binding energy range of 200−1100 eV with a pass energy of 150 eV. High-resolution narrow scans were made at a pass energy of 50 eV, including N_{1s} (395−407 eV) and Cu_{2p} (925−970 eV) spectral regions. The amount of Cu in Cu-*g*-C_3N_4 was measured by an inductively coupled plasma optical emission spectrometer (ICP-OES, Varian, 700-ES, USA).

X-ray Absorption Near-Edge Structure (XANES) Analysis. To determine the bond of Cu in g-C_3N_4 nanosheets, Cu K-edge analysis was done with Si (111) crystal monochromators at the BL11B beamlines at the Shanghai Synchrotron Radiation Facility (SSRF) (Shanghai, China). Powder was pressed into thin sheets of 1 cm diameter and sealed using Kapton tape. The X-ray absorption fine structure (XAFS) spectra were recorded at room temperature using a four-channel silicon drift detector (SDD) Bruker 5040. Cu K-edge extended X-ray absorption fine structure (EXAFS) spectra were recorded in transmission mode and analyzed by the software codes Athena and Artemis. The spectra were normalized to 1, and the background was subtracted using the Athena program from the software package (IFFEFIT). The k^3-weighted $\chi(k)$ data in the *k*-space ranging from 3 to 13 Å^{-1} (multiplied by a Hanning window function with d*k* = 1.0 Å^{-1}) were Fourier transformed to obtain radial distribution functions (R space). In order to determine the detailed structural parameters around Cu atoms in the samples, quantitative curve-fittings were carried out for the Fourier transformed $k^3\chi(k)$ in the R space between 1.2 and 3 Å using the Artemis module of IFEFFIT. Effective backscattering amplitudes $F(k)$ and phase shifts $\Phi(k)$ of all fitting paths were calculated by the ab initio code FEFF 6.0. During the fitting of the Cu-*g*-C_3N_4 powder, the amplitude reduction factor S_0^2 was fixed to the best-fit value of 1.00, and the Cu−N coordination number was fixed to 2.0 while the interatomic distance (R), the Debye−Waller factor (σ^2), and energy shift (δE_0) were allowed to vary. The fit quality was then evaluated using the *R*-factor and reduced Chi-square. The wavelet-transformed EXAFS spectra were obtained using the WTEXAFS program.

Glucose Oxidase-Like Activity. Glucose oxidase-like activities of g-C_3N_4 and Cu-*g*-C_3N_4 were determined by measuring the generation of hydrogen peroxide using *N*,*N*-diethyl-l,4-phenylenediammonium sulfate (DPD) and horseradish peroxidase. First, 100 mg of DPD was dissolved in 10 mL of 0.1 M H_2SO_4 and stored in the dark at 5 °C, for a maximum of 1 week. 10 mg of horseradish peroxidase from horseradish was dissolved in 10 mL of distilled water and stored at 5 °C, for a maximum of 1 week. The glucose oxidation was performed in a quartz cuvette (5 mL) containing different concentrations (1, 2, 4, and 8 mg mL^{-1}) of glucose and 0.2 mg of Cu-*g*-C_3N_4 in 4 mL of PBS (pH 7.0). The photoreaction assay was done in air with irradiation for 10 min ($\lambda \geq 420$ nm) to generate H_2O_2, and the solution was filtered to remove the nanosheets. The CEL-HXF300-T3 xenon lamp (Ceaulight, Beijing, China) was used as the excitation light source to investigate the oxidation of glucose, and the distance between sample and lamp was set to 12 cm, with a 0.2 W cm^{-2} and 420−780 nm irradiation wavelength range. The concentration of generated H_2O_2 was determined by the DPD colorimetric method, as shown in Figure 3a,b. Briefly, 1 mL aliquots containing generated H_2O_2 were mixed with 3 mL of 10 mM phosphate buffer (pH 6), and then 50 μL of DPD solution (10 mg mL^{-1}) and 50 μL horseradish peroxidase (1 mg mL^{-1}) were added to the solution and mixed with pipetting and immediately measured using an UV−vis spectrophotometer. The absorbance at 551 nm was measured to determine the concentration of $DPD^{\bullet+}$ and used for calculating the H_2O_2 generated.[49]

Peroxidase-Like Activity. For the peroxidation reaction, 800 μL of H_2O_2 (0.1, 0.5, 1, 2, 4, and 8 mM) was added to 3.9 mL of acetate buffer (0.1 M, pH 4.2), 200 μL of TMB (12 mM), and 100 μL of Cu-*g*-C_3N_4 (2.5 mg mL^{-1} in PBS, pH 7.4). The mixture was incubated in the dark for 10 min at room temperature and filtered to remove the nanosheets. The absorbance of the solution was measured at 652 nm, and the concentration of the oxidized product of TMB with ε = 39,000 M^{-1} cm^{-1}.[21]

Computational Methods. Theoretical calculations of Cu on g-C_3N_4 nanosheets were carried out with a computational quantum mechanical modeling using the density functional theory to investigate the electronic structure using the Vienna Ab initio Simulation Package (VASP 5.4.4). The projected augmented wave (PAW) method was used to describe the interactions of electrons and ions. The Perdew−Burke−Ernzerhof (PBE) approximation of generalized gradient approximation (GGA) was employed to obtain the exchange and correlation energy. The plane-wave expansion of the Kohn−Sham orbitals was expanded to a kinetic energy cutoff of 450 eV. The convergence criterion of 10^{-4} eV was set for electronic self-consistency, and structural optimizations were processed until the force on each atom was less than 0.02 eV Å^{-1}. The parameters of the unit cell were $a = b = 14.27$ Å, $c = 20$ Å, $\alpha = \beta = 90°$, and $\gamma = 120°$. The 20 Å vacuum layer was added to the surface to eliminate the artificial interactions between periodic images. The weak interaction was described by the DFT+D3 method using empirical correction in Grimme's scheme.[50]

The adsorption energy (E_a) was calculated with the following equation:

$$E_a = E_{comb} - E_c - E_b \quad (2)$$

where E_{comb} stands for the total energy of each metal adsorbed on the nanosheet (-*g*-C_3N_4), E_c represents the energy of g-C_3N_4, and E_b is the energy of each metal.

The Gibbs free energies were calculated from the following equation:

$$\Delta G = \Delta E + \Delta ZPE - T\Delta S \quad (3)$$

where ΔE is the adsorption energy of $\cdot H_2O_2$, $\cdot OH$, and $\cdot O$ on the Cu-*g*-C_3N_4 nanosheet; ΔZPE and ΔS are the zero-point energy change and entropy change of $\cdot H_2O_2$, $\cdot OH$, and $\cdot O$, respectively. T is the temperature (298.15 K).

From density functional theory, adsorption energies can be calculated (eq 2). In this work, adsorption energy refers to the energy necessary for atoms (Fe, Cr, Zn, K, and Cu) to adsorb onto g-C_3N_4 nanosheets and molecules (O_2 and H_2O_2) to adsorb onto g-C_3N_4 and Cu-*g*-C_3N_4 nanosheets. A lower adsorption energy indicates that it is easier for the atoms to adsorb onto g-C_3N_4 nanosheets and molecules to adsorb onto Cu-*g*-C_3N_4. The Gibbs free energy (eq 3) is the thermodynamic potential that is minimized when a system reaches chemical equilibrium. Reaction energy is obtained by calculating the Gibbs free energy change between $\cdot O/\cdot OH$ and $\cdot H_2O_2$ on g-C_3N_4 or Cu-*g*-C_3N_4, and the lower the reaction energy, the easier it is for the reaction to occur.

Bacterial Culturing, Growth Condition, and Harvesting. *Staphylococcus aureus* Xen36 (PerkinElmer, Inc., Waltham, Massachusetts) was grown on tryptone soy agar (TSA, Oxoid, Basingstoke, UK) with 200 μg mL^{-1} kanamycin at 37 °C under aerobic conditions. A single colony was added to 10 mL of tryptone soy broth (TSB) and incubated in humidified air at 37 °C for 24 h and used to inoculate (1:20) main culture (200 mL) and grown for 16 h. Bacterial cultures were harvested by centrifugation for 5 min at 5000*g* and washed twice with PBS (pH 7.4). Bacteria were suspended in PBS to the concentrations required for the experiments as determined by a Bürker-Türk counting chamber.

The multidrug-resistant ESKAPE strains (*Acinetobacter baumannii* 2349, *S. aureus* 6114, *Enterobacter faecium* 1762, *Klebsiella pneumoniae* 6696, *Pseudomonas aeruginosa* 3086, *Enterobacter* 3737) were isolated from patients from the First Affiliated Hospital of Wenzhou Medical University, Wenzhou, China. In the hospital, the ESKAPE strains were tested for multidrug resistance.[51,52] The Gram-positive bacteria were cultured in TSB, and Gram-negative bacteria were cultured in LB. Culturing and harvesting were performed as described above.

For biofilm growth condition, 800 μL of *S. aureus* Xen36 suspension (10^8 bacteria mL^{-1}) was added into a glass-bottom cell culture dish (Φ14 mm) and incubated in humidified air at 37 °C for 1 h to allow the bacteria to adhere to the surface. Next, bacterial suspensions were discarded and washed with 800 μL of PBS to remove unattached bacteria, and 800 μL of TSB was added to each

https://doi.org/10.1021/acsnano.4c12348
ACS Nano 2025, 19, 10816−10828

well and incubated at 37 °C. After 24 h, the culture medium was refreshed and cultured for another 24 h to form biofilms.

Evaluation of Antibacterial Performance with Glucose Oxidase-Like Activity. 100 μL of *S. aureus* Xen36 suspension (2×10^7 bacteria mL^{-1}) in PBS was added to a 96-well plate. Then, 10 μL of glucose (8 mg mL^{-1}) and 90 μL of nanosheet suspension 0, 6.3, 12.5, 25, 50, and 100 μg mL^{-1} in PBS were added to the bacterial suspension. The plate was kept at room temperature with or without irradiation by a xenon lamp for 30 min ($\lambda \geq 420$ nm, 0.2 W cm^{-2}). Then, the bacterial suspension was serially diluted with PBS (pH 7.4), and 10 μL droplets were spotted onto TSB agar plates and incubated in humidified air at 37 °C overnight. CFUs were counted on the agar plates. For the killing efficacy on planktonic bacteria, bacterial suspensions were exposed to PBS, ciprofloxacin (12.5 μg mL^{-1}), Cu-*g*-C_3N_4/light, glucose/light, Cu-*g*-C_3N_4/glucose, and Cu-*g*-C_3N_4/glucose/light for 30 min, the bacteria were spread on an agar plate, and CFUs were enumerated as described above. In addition, the antibacterial performance of g-C_3N_4, Cr-*g*-C_3N_4, Zn-*g*-C_3N_4, Fe-*g*-C_3N_4, and K-*g*-C_3N_4 nanosheets was tested as described above (Figure S1).

Antibacterial performance of Cu-*g*-C_3N_4 was also determined for the ESKAPE panel pathogens. Gram-positive bacteria were cultured in TSB medium, and Gram-negative bacteria were cultured in LB medium (Figure S8).

Protein leakage of the bacteria in the supernatant after exposure to Cu-*g*-C_3N_4 nanosheets was determined using the BCA protein detection kit and followed a previously reported method.[53] Briefly, bacterial suspension exposed to PBS, Cu-*g*-C_3N_4/light, glucose/light, Cu-*g*-C_3N_4/glucose, and Cu-*g*-C_3N_4/glucose/light for 30 min was centrifuged at 5000*g* for 10 min at 4 °C and the protein concentration was determined in the supernatant. Bacteria in PBS without glucose or without light irradiation served as the controls.

FESEM (HITACHI, SU8010, Japan) was used to visualize the interaction of bacteria with the Cu-*g*-C_3N_4 nanosheets. *S. aureus* Xen36 suspensions were exposed to Cu-*g*-C_3N_4, as described above. The exposed bacterial suspension was added onto a silicon wafer (L × W × H, 5 mm × 5 mm × 0.45 mm) in a 48-well plate for 2 h to allow bacterial adhesion. Then, the bacteria were fixed with 4% paraformaldehyde fixative solution (Macklin, Beijing, China) for 40 min and dehydrated with ethanol solutions with increasing concentrations (30, 50, 70, 90, and 100%) for 20 min successively. The silicon wafer was dried at 4 °C, sprayed with gold, and analyzed on a field-emission scanning electron microscope.

The viability of *S. aureus* Xen36 after exposure to Cu-*g*-C_3N_4 nanosheets and ciprofloxacin and PBS as controls, as described above, was evaluated with a Live/Dead BacLight bacterial viability kit. Briefly, the bacteria were stained with SYTO 9 and propidium iodide (PI) for 20 min and analyzed with a Nikon A1 confocal laser scanning microscope (Nikon, A1, Japan). SYTO 9 (green fluorescent determining live bacteria) and PI (red fluorescent determining cell wall damaged bacteria) were excited by the 488 and 561 nm laser, respectively, and their emissions were collected at 500−550 and 570−620 nm. The percentage of SYTO 9-stained and PI-stained bacteria in confocal images was calculated by ImageJ (National Institutes of Health, USA).

Evaluation of Biofilm Eradication Using Cu-*g*-C_3N_4 Nanosheets. *S. aureus* Xen36 biofilms grown on a glass-bottom cell culture dish for 48 h as described above, were exposed to 1 mL Cu-*g*-C_3N_4 nanosheets (12.5 μg mL^{-1}) and glucose (4 mg mL^{-1}) in PBS. The dish was kept at room temperature with or without irradiation by a xenon lamp for 30 min ($\lambda \geq 420$ nm, 0.2 W cm^{-2}). As controls, *S. aureus* Xen36 biofilms were exposed for 30 min in the dark to 1 mL of ciprofloxacin (12.5 μg mL^{-1}) and PBS. Biofilms were stained with SYTO 9/PI for 30 min as described above and then imaged with confocal laser scanning microscopy.

Evaluation of Antibacterial Properties of Cu-*g*-C_3N_4/PCL Nanofibers *In Vitro*. Cu-*g*-C_3N_4/PCL (1 mg, 10 mm diameter, 1 mm thickness) at different concentrations were added to 190 μL of *S. aureus* Xen36 (10^7 mL^{-1}) in PBS in a 48-well plate. 10 μL of glucose (80 mg mL^{-1}) was then added into each well at the final concentration of 4 mg mL^{-1}. The plate was illuminated by a light source for 30 min ($\lambda \geq 420$ nm, 0.2 W cm^{-2}); PBS without nanofibers were used as controls. The resultant bacterial suspension was serially diluted with PBS, and 10 μL droplets were spotted onto TSB agar plates and incubated at 37 °C overnight. CFUs were enumerated on the agar plates.

Infected Murine Wound Model and Evaluation of Wound Healing with Cu-*g*-C_3N_4/PCL Dressings. Forty ICR female mice (6−8 weeks, 20−30 g) were purchased from Zhejiang Vital River Laboratory Animal Technology Co., Ltd., and housed in a specific-pathogen-free room. The animal experimental protocols were reviewed and approved by the Institutional Animal Care and User Committee, Wenzhou Institute, University of Chinese Academy of Sciences. The hind part of ICR female mice was shaved, and a circular, full-thickness skin wound with a diameter of 6 mm was made by a sterilized puncher (TEN-WIN). The wounds were then inoculated with *S. aureus* Xen36 (10 μL, 10^{11} bacteria mL^{-1}) in PBS and randomly divided into four groups (eight mice per group). After 24 h (day 0), mice were anesthetized, and the wounds were treated with PBS (control), ciprofloxacin (10 μL, 12.5 μg mL^{-1}), Cu-*g*-C_3N_4/PCL/light (5 mm-diameter Cu-*g*-C_3N_4/PCL with 10 min light irradiation ($\lambda \geq 420$ nm, 0.2 W cm^{-2})), Cu-*g*-C_3N_4/PCL/glucose (5 mm-diameter Cu-*g*-C_3N_4/PCL, 4 mg mL^{-1} glucose in the dark), and Cu-*g*-C_3N_4/PCL/glucose/light (5 mm-diameter Cu-*g*-C_3N_4/PCL, 4 mg mL^{-1} glucose with l0 min light irradiation ($\lambda \geq 420$ nm, 0.2 W cm^{-2})). At different time intervals (day 0, 1, 2, 6, 10, and 14), the bioluminescent images of the wounds were recorded by the IVIS Lumina XRMS Series III bio-optical imaging system (PerkinElmer, exposure time: 30 s, binning factor: 4, 1 F/Stop, open emission filter). Regions of interest were manually created for each image, and bioluminescence intensity was calculated. The wound sizes of the mice were recorded on days 0, 1, 2, 6, 10, and 14, and the wound area was measured and calculated by ImageJ (National Institutes of Health, USA).

In a parallel study, on day 2 post-treatment, three mice in each group were sacrificed, and the wound tissues were collected and immersed in PBS. The tissues were homogenized by using an ultrasonic cell pulverizer (HN150-Y, Hannuo). Meanwhile, inflammatory factors (IL-1*β*, IL-6, TNF-*α*, and IL-10) in wound tissue were determined using enzyme-linked immunosorbent assay (ELISA kit) following the manufacturer's instructions, and the optical density (OD) value at 450 nm was measured with a microplate reader (Epoch2). The homogenized tissues were serially diluted with PBS and 10 μL droplets were spotted on TSB agar plates and cultured in humidified air at 37 °C overnight. CFUs were enumerated on the agar plates.

On day 14 post-treatment, all mice were sacrificed. Wound tissue and organs (heart, liver, spleen, lung, kidney) of the mice were fixed in 10% formalin, decalcified (wound tissue), embedded in paraffin, and sectioned in slices with a thickness of 5 μm; the slices were stained with hematoxylin and eosin (H&E) and Masson staining as previously published.[54] The hematoxylin and eosin stain the nucleus (blue) and cytoplasm (red) to observe inflammatory cells. Masson staining shows a clear view of collagen fibers deposition and reorganization (blue).

Statistical Analysis. All experiments were carried out in triplicate with separately cultured bacteria or cells. Results were expressed as means ± standard deviations (SD) and analyzed with one-way analysis of variance (ANOVA), followed by Dunnett's or Tukey's test for multiple comparison using GraphPad Prism 8.0 (Dotmatics). Differences between groups at $p < 0.05$ were considered as statistically significant.

ASSOCIATED CONTENT

Supporting Information

The Supporting Information is available free of charge at https://pubs.acs.org/doi/10.1021/acsnano.4c12348.

Additional experimental methods; DFT, UV−vis, and antibacterial test of different metal atoms on g-C_3N_4; TEM of g-C_3N_4 bulk and nanosheets; XRD, XPS, H_2O_2

https://doi.org/10.1021/acsnano.4c12348
ACS Nano 2025, 19, 10816−10828

generation, •OH detection, multidrug resistance, and cell viability of Cu-*g*-C_3N_4; wound image and H&E/Masson tissue staining after treatment by Cu-*g*-C_3N_4/PCL); and Cu K-edge EXAFS fits and Gibbs free energy value (DOCX)

AUTHOR INFORMATION

Corresponding Authors

Linqi Shi − *State Key Laboratory of Medicinal Chemical Biology, Key Laboratory of Functional Polymer Materials, Ministry of Education, Institute of Polymer Chemistry, College of Chemistry, Nankai University, Tianjin 300071, China;* orcid.org/0000-0002-9534-795X; Email: shilinqi@nankai.edu.cn

Henny C. van der Mei − *Department of Biomaterials & Biomedical Technology, University of Groningen and University Medical Center Groningen, Groningen 9713 AV, The Netherlands;* orcid.org/0000-0003-0760-8900; Email: h.c.van.der.mei@umcg.nl

Yong Liu − *Translational Medicine Laboratory, the First Affiliated Hospital of Wenzhou Medical University, Wenzhou, Zhejiang 325035, China; State Key Laboratory of Medicinal Chemical Biology, Key Laboratory of Functional Polymer Materials, Ministry of Education, Institute of Polymer Chemistry, College of Chemistry, Nankai University, Tianjin 300071, China;* orcid.org/0000-0003-1738-7857; Email: y.liu@nankai.edu.cn

Authors

Fan Wu − *Translational Medicine Laboratory, the First Affiliated Hospital of Wenzhou Medical University, Wenzhou, Zhejiang 325035, China; Department of Biomaterials & Biomedical Technology, University of Groningen and University Medical Center Groningen, Groningen 9713 AV, The Netherlands; State Key Laboratory of Medicinal Chemical Biology, Key Laboratory of Functional Polymer Materials, Ministry of Education, Institute of Polymer Chemistry, College of Chemistry, Nankai University, Tianjin 300071, China*

Yaran Wang − *Translational Medicine Laboratory, the First Affiliated Hospital of Wenzhou Medical University, Wenzhou, Zhejiang 325035, China; Department of Biomaterials & Biomedical Technology, University of Groningen and University Medical Center Groningen, Groningen 9713 AV, The Netherlands; State Key Laboratory of Medicinal Chemical Biology, Key Laboratory of Functional Polymer Materials, Ministry of Education, Institute of Polymer Chemistry, College of Chemistry, Nankai University, Tianjin 300071, China*

Yuanfeng Li − *Translational Medicine Laboratory, the First Affiliated Hospital of Wenzhou Medical University, Wenzhou, Zhejiang 325035, China*

Lu Yuan − *Department of Biomaterials & Biomedical Technology, University of Groningen and University Medical Center Groningen, Groningen 9713 AV, The Netherlands*

Yijin Ren − *Department of Orthodontics, University of Groningen and University Medical Center Groningen, Groningen 9700 RB, The Netherlands*

Complete contact information is available at: https://pubs.acs.org/10.1021/acsnano.4c12348

Author Contributions

F.W., Yu.L., L.S., and Yo.L. conceived the research. F.W., Y.W., and Yo.L. developed, prepared, and characterized materials. F.W., Yu.L., L.Y., Y.R., H.C.v.d.M., and Yo.L. wrote and revised the manuscript. H.C.v.d.M. and Yo.L. supervised the research. All authors read and commented on the manuscript.

Notes

The authors declare no competing financial interest.

ACKNOWLEDGMENTS

This work was financially supported by the National Natural Science Foundation of China (Grant Nos. 52293383 (L.S.), 22275043 (Y.Liu), and 52203184 (Y.Li)); the National Key R&D Program (Grant No. 2023YFB3809902); Zhejiang Provincial Natural Science Foundation Outstanding Youth Project (LR24H180001); Startup Fund of Wenzhou Institute, University of Chinese Academy of Sciences (Grant No. WIUCASQD2021022); and the University Medical Center Groningen.

REFERENCES

(1) Durand-Reville, T. F.; Miller, A. A.; O'Donnell, J. P.; Wu, X.; Sylvester, M. A.; Guler, S.; Iyer, R.; Shapiro, A. B.; Carter, N. M.; Velez-Vega, C.; Moussa, S. H.; McLeod, S. M.; Chen, A.; Tanudra, A. M.; Zhang, J.; Comita-Prevoir, J.; Romero, J. A.; Huynh, H.; Ferguson, A. D.; Horanyi, P. S.; Mayclin, S. J.; Heine, H. S.; Drusano, G. L.; Cummings, J. E.; Slayden, R. A.; Tommasi, R. A. Rational Design of a New Antibiotic Class for Drug-Resistant Infections. *Nature* **2021**, *597*, 698−702.

(2) Wang, X.; Xu, X.; Zhang, S.; Chen, N.; Sun, Y.; Ma, K.; Hong, D.; Li, L.; Du, Y.; Lu, X.; Jiang, S. TPGS-Based and S-Thanatin Functionalized Nanorods for Overcoming Drug Resistance in *Klebsiella pneumonia*. *Nat. Commun.* **2022**, *13*, 3731.

(3) Abrigo, M.; McArthur, S. L.; Kingshott, P. Electrospun Nanofibers as Dressings for Chronic Wound Care: Advances, Challenges, and Future Prospects. *Macromol. Biosci.* **2014**, *14*, 772−792.

(4) Desrousseaux, C.; Sautou, V.; Descamps, S.; Traoré, O. Modification of the Surfaces of Medical Devices to Prevent Microbial Adhesion and Biofilm Formation. *J. Hosp. Infect.* **2013**, *85*, 87−93.

(5) Qin, B.; Fei, C.; Bridges, A. A.; Mashruwala, A. A.; Stone, H. A.; Wingreen, N. S.; Bassler, B. L. Cell Position Fates and Collective Fountain Flow in Bacterial Biofilms Revealed by Light-Sheet Microscopy. *Science* **2020**, *369*, 71−77.

(6) Berne, C.; Ellison, C. K.; Ducret, A.; Brun, Y. V. Bacterial Adhesion at the Single-Cell Level. *Nat. Rev. Microbiol.* **2018**, *16*, 616−627.

(7) Mejía-Salazar, J. R.; Oliveira, O. N. Plasmonic Biosensing. *Chem. Rev.* **2018**, *118*, 10617−10625.

(8) Flemming, H.-C.; Wingender, J.; Szewzyk, U.; Steinberg, P.; Rice, S. A.; Kjelleberg, S. Biofilms: An Emergent Form of Bacterial Life. *Nat. Rev. Microbiol.* **2016**, *14*, 563−575.

(9) Stewart, P. S.; William Costerton, J. Antibiotic Resistance of Bacteria in Biofilms. *Lancet* **2001**, *358*, 135−138.

(10) Li, Y.; Su, L.; Zhang, Y.; Liu, Y.; Huang, F.; Ren, Y.; An, Y.; Shi, L.; Van der Mei, H. C.; Busscher, H. J. A Guanosine-Quadruplex Hydrogel as Cascade Reaction Container Consuming Endogenous Glucose for Infected Wound Treatment—A Study in Diabetic Mice. *Adv. Sci.* **2022**, *9*, No. 2103485.

(11) Chen, L.; Peng, M.; Li, H.; Zhou, J.; He, W.; Hu, R.; Ye, F.; Li, Y.; Shi, L.; Liu, Y. Metal-Phenolic Network with Pd Nanoparticle Nodes Synergizes Oxidase-Like and Photothermal Properties to Eradicate Oral Polymicrobial Biofilm-Associated Infections. *Adv. Mater.* **2024**, *36*, No. 2306376.

(12) Wang, C.; Yue, L.; Willner, I. Controlling Biocatalytic Cascades with Enzyme−DNA Dynamic Networks. *Nat. Catal.* **2020**, *3*, 941−950.

(13) Chen, L.; Chen, Y.; Zhang, R.; Yu, Q.; Liu, Y.; Liu, Y. Glucose-Activated Nanoconfinement Supramolecular Cascade Reaction In Situ for Diabetic Wound Healing. *ACS Nano* **2022**, *16*, 9929−9937.
(14) Wang, Q.; Wei, H.; Zhang, Z.; Wang, E.; Dong, S. Nanozyme: An Emerging Alternative to Natural Enzyme for Biosensing and Immunoassay. *TrAC Trends Anal. Chem.* **2018**, *105*, 218−224.
(15) Wang, H.; Wan, K.; Shi, X. Recent Advances in Nanozyme Research. *Adv. Mater.* **2019**, *31*, No. 1805368.
(16) Wu, J.; Wang, X.; Wang, Q.; Lou, Z.; Li, S.; Zhu, Y.; Qin, L.; Wei, H. Nanomaterials with Enzyme-like Characteristics (Nanozymes): Next-Generation Artificial Enzymes (II). *Chem. Soc. Rev.* **2019**, *48*, 1004−1076.
(17) Xu, G.; Ren, Z.; Xu, J.; Lu, H.; Liu, X.; Qu, Y.; Li, W.; Zhao, M.; Huang, W.; Li, Y.-Q. Organic−Inorganic Heterointerface-Expediting Electron Transfer Realizes Efficient Plasmonic Catalytic Sterilization via a Carbon-Dot Nanozyme. *ACS Appl. Mater. Interfaces* **2024**, *16*, 21689−21698.
(18) Xu, G.; Liu, K.; Jia, B.; Dong, Z.; Zhang, C.; Liu, X.; Qu, Y.; Li, W.; Zhao, M.; Zhou, H.; Li, Y.-Q. Electron Lock Manipulates the Catalytic Selectivity of Nanozyme. *ACS Nano* **2024**, *18*, 3814−3825.
(19) El-Kady, M. F.; Shao, Y.; Kaner, R. B. Graphene for Batteries, Supercapacitors and Beyond. *Nat. Rev. Mater.* **2016**, *1*, 16033.
(20) Wang, Z.; Jin, B.; Peng, J.; Su, W.; Zhang, K.; Hu, X.; Wang, G.; Park, J. H. Engineered Polymeric Carbon Nitride Additive for Energy Storage Materials: A Review. *Adv. Funct. Mater.* **2021**, *31*, No. 2102300.
(21) Zhang, P.; Sun, D.; Cho, A.; Weon, S.; Lee, S.; Lee, J.; Han, J. W.; Kim, D.-P.; Choi, W. Modified Carbon Nitride Nanozyme as Bifunctional Glucose Oxidase-Peroxidase for Metal-Free Bioinspired Cascade Photocatalysis. *Nat. Commun.* **2019**, *10*, 940.
(22) Sengupta, P.; Pramanik, K.; Datta, P.; Sarkar, P. Chemically Modified Carbon Nitride-Chitin-Acetic Acid Hybrid as a Metal-Free Bifunctional Nanozyme Cascade of Glucose Oxidase-Peroxidase for "Click off" Colorimetric Detection of Peroxide and Glucose. *Biosens. Bioelectron.* **2020**, *154*, No. 112072.
(23) Li, L.; Hu, Y.; Shi, Y.; Liu, Y.; Liu, T.; Zhou, H.; Niu, W.; Zhang, L.; Zhang, J.; Xu, G. Triple-Enzyme-Mimicking $AuPt_3Cu$ Hetero-Structural Alloy Nanozymes towards Cascade Reactions in Chemodynamic Therapy. *Chem. Eng. J.* **2023**, *463*, No. 142494.
(24) Wang, X.; Maeda, K.; Thomas, A.; Takanabe, K.; Xin, G.; Carlsson, J. M.; Domen, K.; Antonietti, M. A Metal-Free Polymeric Photocatalyst for Hydrogen Production from Water under Visible Light. *Nat. Mater.* **2009**, *8*, 76−80.
(25) Ju, E.; Dong, K.; Chen, Z.; Liu, Z.; Liu, C.; Huang, Y.; Wang, Z.; Pu, F.; Ren, J.; Qu, X. Copper(II)−Graphitic Carbon Nitride Triggered Synergy: Improved ROS Generation and Reduced Glutathione Levels for Enhanced Photodynamic Therapy. *Angew. Chemie Int. Ed.* **2016**, *55*, 11467−11471.
(26) Xia, P.; Antonietti, M.; Zhu, B.; Heil, T.; Yu, J.; Cao, S. Designing Defective Crystalline Carbon Nitride to Enable Selective CO_2 Photoreduction in the Gas Phase. *Adv. Funct. Mater.* **2019**, *29*, No. 1900093.
(27) Mane, G. P.; Talapaneni, S. N.; Lakhi, K. S.; Ilbeygi, H.; Ravon, U.; Al-Bahily, K.; Mori, T.; Park, D.-H.; Vinu, A. Highly Ordered Nitrogen-Rich Mesoporous Carbon Nitrides and their Superior Performance for Sensing and Photocatalytic Hydrogen Generation. *Angew. Chemie Int. Ed.* **2017**, *56*, 8481−8485.
(28) Wang, W.; Bai, X.; Ci, Q.; Du, L.; Ren, X.; Phillips, D. L. Near-Field Drives Long-Lived Shallow Trapping of Polymeric C_3N_4 for Efficient Photocatalytic Hydrogen Evolution. *Adv. Funct. Mater.* **2021**, *31*, No. 2103978.
(29) Wakerley, D.; Lamaison, S.; Ozanam, F.; Menguy, N.; Mercier, D.; Marcus, P.; Fontecave, M.; Mougel, V. Bio-Inspired Hydrophobicity Promotes CO_2 Reduction on a Cu Surface. *Nat. Mater.* **2019**, *18*, 1222−1227.
(30) Lu, J.; Wang, J.; Zou, Q.; He, D.; Zhang, L.; Xu, Z.; He, S.; Luo, Y. Unravelling the Nature of the Active Species as well as the Doping Effect over Cu/Ce-Based Catalyst for Carbon Monoxide Preferential Oxidation. *ACS Catal.* **2019**, *9*, 2177−2195.
(31) Yang, J.; Huang, Y.; Chen, Y.-W.; Xia, D.; Mou, C.-Y.; Hu, L.; Zeng, J.; He, C.; Wong, P. K.; Zhu, H.-Y. Active Site-Directed Tandem Catalysis on $CuO/VO\text{-}MnO_2$ for Efficient and Stable Catalytic Ozonation of S-VOCs under Mild Condition. *Nano Today* **2020**, *35*, No. 100944.
(32) Xie, F.; Cui, X.; Zhi, X.; Yao, D.; Johannessen, B.; Lin, T.; Tang, J.; Woodfield, T. B. F.; Gu, L.; Qiao, S.-Z. A General Approach to 3D-Printed Single-Atom Catalysts. *Nat. Synth.* **2023**, *2*, 129−139.
(33) Chen, Z.; Zhao, J.; Cabrera, C. R.; Chen, Z. Computational Screening of Efficient Single-Atom Catalysts Based on Graphitic Carbon Nitride ($g\text{-}C_3N_4$) for Nitrogen Electroreduction. *Small Methods* **2019**, *3*, No. 1800368.
(34) Xue, T.; Peng, B.; Xue, M.; Zhong, X.; Chiu, C.-Y.; Yang, S.; Qu, Y.; Ruan, L.; Jiang, S.; Dubin, S.; Kaner, R. B.; Zink, J. I.; Meyerhoff, M. E.; Duan, X.; Huang, Y. Integration of Molecular and Enzymatic Catalysts on Graphene for Biomimetic Generation of Antithrombotic Species. *Nat. Commun.* **2014**, *5*, 3200.
(35) Völler, J.-S. Biocatalytic Hollow Inorganic Spheres. *Nat. Catal.* **2023**, *6*, 979.
(36) Qiao, Q.; Wang, J.; Long, K.; Li, L.; Chen, J.; Guo, Y.; Xu, Z.; Kuang, Y.; Ji, T.; Li, C. A Cascaded Enzyme System Based on the Catalase-like Activity of $Ti_3C_2T_x$ MXene Nanosheets for the Efficient Combination Cancer Therapy. *Nano Today* **2024**, *54*, No. 102059.
(37) Chen, L.; Peng, M.; Zhou, J.; Hu, X.; Piao, Y.; Li, H.; Hu, R.; Li, Y.; Shi, L. L.; Liu, Y. Supramolecular Photothermal Cascade Nanoreactor Enables Photothermal Effect, Cascade Reaction, and In Situ Hydrogelation for Biofilm-Associated Tooth-Extraction Wound Healing. *Adv. Mater.* **2023**, *35*, No. 2301664.
(38) Xu, B.; Wang, H.; Wang, W.; Gao, L.; Li, S.; Pan, X.; Wang, H.; Yang, H.; Meng, X.; Wu, Q.; Zheng, L.; Chen, S.; Shi, X.; Fan, K.; Yan, X.; Liu, H. A Single-Atom Nanozyme for Wound Disinfection Applications. *Angew. Chemie-International Ed.* **2019**, *58*, 4911−4916.
(39) Ji, S.; Jiang, B.; Hao, H.; Chen, Y.; Dong, J.; Mao, Y.; Zhang, Z.; Gao, R.; Chen, W.; Zhang, R.; Liang, Q.; Li, H.; Liu, S.; Wang, Y.; Zhang, Q.; Gu, L.; Duan, D.; Liang, M.; Wang, D.; Yan, X.; Li, Y. Matching the Kinetics of Natural Enzymes with a Single-Atom Iron Nanozyme. *Nat. Catal.* **2021**, *4*, 407−417.
(40) Ou, C.; Yang, F.; Gong, M.; Xu, C.; Yang, S.; Yang, J.; Qi, W.; Luo, Y.; Peng, Z.; Deng, L.; He, D. Enhancing Enzymatic Activity of Glucose Oxidase by Metal−Organic Framework Nanocarriers for Intensive Cascade Catalytic Antibacterial Therapy. *ACS Appl. Nano Mater.* **2023**, *6*, 15860−15870.
(41) Qu, L.; Fang, X.; Xie, T.; Xu, H.; Yang, G.; Liu, W. Nanozyme-Catalyzed Cascade Reactions for High-Sensitive Glucose Sensing and Efficient Bacterial Killing. *Sensors Actuators B Chem.* **2022**, *353*, No. 131156.
(42) Uberoi, A.; McCready-Vangi, A.; Grice, E. A. The Wound Microbiota: Microbial Mechanisms of Impaired Wound Healing and Infection. *Nat. Rev. Microbiol.* **2024**, *22*, 507−521.
(43) Xu, W.; Chen, Y.; Zhang, B.; Xu, W.; Niu, J.; Liu, Y. Supramolecular Assembly of *β*-Cyclodextrin-Modified Polymer by Electrospinning with Sustained Antibacterial Activity. *Biomacromolecules* **2021**, *22*, 4434−4445.
(44) Jiang, Y.; Dong, K.; An, J.; Liang, F.; Yi, J.; Peng, X.; Ning, C.; Ye, C.; Wang, Z. L. UV-Protective, Self-Cleaning, and Antibacterial Nanofiber-Based Triboelectric Nanogenerators for Self-Powered Human Motion Monitoring. *ACS Appl. Mater. Interfaces* **2021**, *13*, 11205−11214.
(45) Güemes, M.; Rahman, S. A.; Hussain, K. What Is a Normal Blood Glucose? *Arch. Dis. Child.* **2016**, *101*, 569−574.
(46) ElSayed, N. A.; Aleppo, G.; Bannuru, R. R.; Bruemmer, D.; Collins, B. S.; Ekhlaspour, L.; Gaglia, J. L.; Hilliard, M. E.; Johnson, E. L.; Khunti, K.; Lingvay, I.; Matfin, G.; McCoy, R. G.; Perry, M. L.; Pilla, S. J.; Polsky, S.; Prahalad, P.; Pratley, R. E.; Segal, A. R.; Seley, J. J.; Selvin, E.; Stanton, R. C.; Gabbay, R. A.; American Diabetes Association Professional Practice Committee. 2. Diagnosis and Classification of Diabetes: Standards of Care in Diabetes-2024. *Diabetes Care* **2024**, *47*, S20−S42.

https://doi.org/10.1021/acsnano.4c12348
ACS Nano 2025, 19, 10816−10828

(47) Tang, S.-C.; Chiu, Y.-C.; Hsu, C.-T.; Peng, S.-J.; Fu, Y.-Y. Plasticity of Schwann Cells and Pericytes in Response to Islet Injury in Mice. *Diabetologia* **2013**, *56*, 2424−2434.
(48) Ma, M.; Huang, Z.; Doronkin, D. E.; Fa, W.; Rao, Z.; Zou, Y.; Wang, R.; Zhong, Y.; Cao, Y.; Zhang, R.; Zhou, Y. Ultrahigh Surface Density of Co-N_2C Single-Atom-Sites for Boosting Photocatalytic CO_2 Reduction to Methanol. *Appl. Catal. B Environ.* **2022**, *300*, No. 120695.
(49) Gao, L.; Zhuang, J.; Nie, L.; Zhang, J.; Zhang, Y.; Gu, N.; Wang, T.; Feng, J.; Yang, D.; Perrett, S.; Yan, X. Intrinsic Peroxidase-like Activity of Ferromagnetic Nanoparticles. *Nat. Nanotechnol.* **2007**, *2*, 577−583.
(50) Grimme, S.; Antony, J.; Ehrlich, S.; Krieg, H. A Consistent and Accurate Ab Initio Parametrization of Density Functional Dispersion Correction (DFT-D) for the 94 Elements H-Pu. *J. Chem. Phys.* **2010**, *132*, No. 154104.
(51) Wang, L.; Zhang, Y.; Lin, Y.; Cao, J.; Xu, C.; Chen, L.; Wang, Y.; Sun, Y.; Zheng, X.; Liu, Y.; Zhou, T.; Carvalho-Assef, A. P. D. Resveratrol Increases Sensitivity of Clinical Colistin-Resistant *Pseudomonas aeruginosa* to Colistin In Vitro and In Vivo. *Microbiol. Spectrum* **2023**, *11*, No. e01992-22.
(52) Yao, Z.; Feng, L.; Zhao, Y.; Zhang, X.; Chen, L.; Wang, L.; Zhang, Y.; Sun, Y.; Zhou, T.; Cao, J.; Frances Yap, M. N. Thymol Increases Sensitivity of Clinical Col-R Gram-Negative Bacteria to Colistin. *Microbiol. Spectr.* **2022**, *10*, 1−22.
(53) Li, Y.; Liu, X.; Tan, L.; Cui, Z.; Jing, D.; Yang, X.; Liang, Y.; Li, Z.; Zhu, S.; Zheng, Y.; Yeung, K. W. K.; Zheng, D.; Wang, X.; Wu, S. Eradicating Multidrug-Resistant Bacteria Rapidly Using a Multi Functional g-C_3N_4@Bi_2S_3 Nanorod Heterojunction with or without Antibiotics. *Adv. Funct. Mater.* **2019**, *29*, No. 1900946.
(54) Suvika, A.; Effendy, A. W. M. The Use of Modified Masson's Trichrome Staining in Collagen Evaluation in Wound Healing Study. *Malays. J. Vet. Res.* **2012**, *3*, 39−47.

https://doi.org/10.1021/acsnano.4c12348
ACS Nano 2025, 19, 10816−10828